Journal of Zhejiang University-SCIENCE A (Applied Physics & Engineering) 2024 25(2):97-115
www.jzus.zju.edu.cn; www.springer.com/journal/11582
E-mail: jzus_a@zju.edu.cn

Research Article

https://doi.org/10.1631/jzus.A2300476

Stress relaxation properties of calcium silicate hydrate: a molecular dynamics study

Zhicheng GENG[1], Shengwen TANG[1,2]✉, Yang WANG[1], Hubao A[1], Zhen HE[1], Kai WU[2], Lei WANG[3]

[1]*State Key Laboratory of Water Resources Engineering and Management, Wuhan University, Wuhan 430072, China*
[2]*Key Laboratory of Advanced Civil Engineering Materials of Ministry of Education, School of Materials Science and Engineering, Tongji University, Shanghai 200092, China*
[3]*College of Materials Science and Engineering, Xi'an University of Architecture and Technology, Xi'an 710055, China*

Abstract: The time-dependent viscoelastic response of cement-based materials to applied deformation is far from fully understood at the atomic level. Calcium silicate hydrate (C-S-H), the main hydration product of Portland cement, is responsible for the viscoelastic mechanism of cement-based materials. In this study, a molecular model of C-S-H was developed to explain the stress relaxation characteristics of C-S-H at different initial deformation states, Ca/Si ratios, temperatures, and water contents, which cannot be accessed experimentally. The stress relaxation of C-S-H occurs regardless of whether it is subjected to initial shear, tensile, or compressive deformation, and shows a heterogeneous characteristic. Water plays a crucial role in the stress relaxation process. A large Ca/Si ratio and high temperature reduce the cohesion between the calcium-silicate layer and the interlayer region, and the viscosity of the interlayer region, thereby accelerating the stress relaxation of C-S-H. The effect of the hydrogen bond network and the morphology of C-S-H on the evolution of the stress relaxation characteristics of C-S-H at different water contents was elucidated by nonaffine mean squared displacement. Our results shed light on the stress relaxation characteristics of C-S-H from a microscopic perspective, bridging the gap between the microscopic phenomena and the underlying atomic-level mechanisms.

Key words: Calcium silicate hydrate (C-S-H); Stress relaxation; Ca/Si ratio; Temperature; Water content; Atomic simulation

1 Introduction

Concrete is one of the most widely used materials in the world, and a better knowledge of its long-term behavior is essential for sustainability as well as for the damage prevention and optimal design of civil engineering structures (Gao et al., 2013; Giorla and Dunant, 2018; Fang and Zhang, 2020; Du and Pang, 2021). Its viscoelasticity plays a critical role in structures with a long service life such as hydropower plants, thus determining the long-term behavior of concrete. The viscoelasticity is referred to as creep and stress relaxation, which induces the redistribution of stress inside concrete (Brooks and Neville, 1976). The stress relaxation phenomenon can be described as the gradual reduction of stress under constant initial deformation. The stress relaxation plays a significant role in the reduction of tensile stress and stress rate of concrete, thus reducing the autogenous shrinkage and the cracking potential of concrete at an early age (Zhang and Qin, 2006; Fu et al., 2015; Atutis et al., 2018; Li ZM et al., 2020; Rong et al., 2021). In recent decades, the stress relaxation behavior of concrete has been extensively investigated. Li et al. (2018) used the finite element method to predict the long-term properties of cement paste and found that the stress-induced dissolution of solid constituents was associated with the stress/strain levels and the selected region. Frech-Baronet et al. (2017), through numerous micro-indentation tests on cement paste, found that in the 30%–85% relative humidity range, higher relative humidity led to a higher relaxation rate of cement paste. Giorla and Dunant (2018) showed by means of finite element simulation that certain micro cracks in cement paste could accelerate the stress relaxation of

✉ Shengwen TANG, tangsw@whu.edu.cn
Shengwen TANG, https://orcid.org/0000-0002-4883-3103

Received Sept. 19, 2023; Revision accepted Nov. 27, 2023;
Crosschecked Dec. 28, 2023

concrete. Despite extensive studies of the stress relaxation behavior of concrete, its underlying mechanism is not fully understood. It has been widely accepted that intrinsic time-dependent deformation within calcium silicate hydrate (C-S-H) gel, which is generally nearly amorphous, accounts for the main mechanism of stress relaxation of cement paste (Feldman, 1972; Tamtsia and Beaudoin, 2000; Vandewalle et al., 2002; Chen and Qian, 2017; Hou et al., 2018a; Ding and Chen, 2019). As the main binding phase and hydration product in cement paste, C-S-H is perhaps the most widely used amorphous material, exhibiting the ubiquitous characteristics of long-range disorder and short-range order. The Ca/Si ratio (molar ratio) of C-S-H in hydrated Portland cement is usually in the range of 1.5–2.0 with a mean value of about 1.7 (Richardson, 1999). However, to improve the durability of cement-based materials, various supplementary cementitious materials are used, resulting in a change in the Ca/Si ratio of C-S-H (Lothenbach et al., 2011). There have been many theories associated with C-S-H gel accounting for the stress relaxation of concrete, such as the viscous shear theory, the seepage theory, and the microprestress relaxation theory (Bažant et al., 1997; Maruyama et al., 2015; Liu et al., 2020). However, since some of these theories are based on assumptions and lack an appropriate understanding of the nano-structural characteristics of cement paste, most of them relate to the macro level, and it is still a challenge to describe where and how stress relaxation occurs. There are many other physical and chemical behaviors that occur during the process of stress relaxation, such as the nano-diffusion of water molecules in C-S-H gel, rearrangement of cement paste gel, and dissolution of load-bearing phases (Bazant and Chern, 1985; Jennings, 2004; Zhang et al., 2011; Li et al., 2015; Frech-Baronet et al., 2017). Therefore, it is difficult to investigate the stress relaxation behavior separately. In addition, some factors such as temperature, relative humidity, and water content, cannot be adequately explained by direct insights at the molecular level related to the stress relaxation behavior of C-S-H gel.

Molecular dynamics (MD) simulation is a very powerful method of computational chemistry for analyzing the physical motions of atoms or molecules within a system. It can be also used to investigate the structure, dynamics, and interfacial behavior of C-S-H gel (Scrivener and Kirkpatrick, 2008; Hou et al., 2018b). It is believed that MD can bridge simulation-based first-principle method and continuum method, helping gain a fundamental understanding of experimental phenomena at the atomic level, and providing valuable information that cannot be obtained from conventional experiments (Talebi et al., 2014; Shishegaran et al., 2020; Zhang et al., 2021). In recent decades, MD has been used to study the stress relaxation characteristics of numerous materials, such as vitrimers, polymers, and metals. Ciarella et al. (2018) proposed an MD coarse-grained model of vitrimers and proposed that some topological defects accelerated the stress relaxation. Chen et al. (2022) investigated the stress relaxation behavior of a SiO_2/Si bilayer composite by nanoindentation with a finite indentation depth of 5.6 nm. Yang et al. (2016) studied the effect of size and temperature on the stress relaxation characteristics of copper using MD and experiments, and developed a formula to describe time, stress, and temperature-dependent deformation. For C-S-H gel, since Pellenq et al. (2009) proposed a realistic molecular structure of C-S-H with a Ca/Si ratio of 1.65, studies of C-S-H using MD have been further developed. Abdolhosseini Qomi et al. (2014) proposed a combinatorial approach to build the atomic structure of C-S-H with a Ca/Si ratio ranging from 1.1 to 2.1 to optimize the mechanical properties of cement paste at nanoscale. Due to its amorphous structure, it is quite hard to determine the morphology of C-S-H gel. However, at the atomic level, it is widely accepted that C-S-H presents seemingly a layered-like structure. In addition, to describe the interactions among atoms within the C-S-H model, the potential of force fields such as ClayFF, CSHFF, and ReaxFF has been developed (Cygan et al., 2004; Shahsavari et al., 2011; Manzano et al., 2012; Pitman and van Duin, 2012). CSHFF potential is a modified version of ClayFF, demonstrating a better prediction ability than ClayFF (Shahsavari et al., 2011). CSHFF potential has been widely accepted in the simulation of cement-based materials. For example, Kai et al. (2021) found that high temperature and interlayer water content could accelerate the creep of C-S-H, based on this force field. Youssef et al. (2011) studied the structural and dynamic properties of water ultra-confined in the nanopores of highly disordered C-S-H. Arayro et al. (2018) found that cesium ions had little effect on the

elastic property of C-S-H according to the effect of cesium sorption on cement paste.

While there have been many studies of the viscoelasticity of C-S-H, most have focused on its creep behavior and few on its stress relaxation behavior. Therefore, there is still a huge gap in understanding the stress relaxation response of C-S-H at the molecular level and providing a reasonable explanation for the experimental phenomenon. In addition, some influencing factors of the stress relaxation of C-S-H, such as the applied initial deformation states (shear, tensile, and compressive modes), initial deformation magnitude, temperature, Ca/Si ratios, and water contents, have not been fully investigated at the atomic level.

To bridge the gap between atomic simulation and the microstructural phenomena presented in experiments, molecular simulation was used in this study to investigate the stress relaxation characteristics of the C-S-H molecular structure at different initial deformation states, Ca/Si ratios (1.3, 1.7, and 1.9), temperatures (298, 373, and 423 K), and interlayer water contents (0%, 30%, 50%, 70%, and 100%). In the stress relaxation process, the atomic dynamics were evaluated by the mean squared displacements (MSDs), the chemical characteristics of bond strength by the time correction function $C(t)$, and the structural characteristics by the nonaffine mean squared displacements ($D^2_{\min}$).

2 Simulation method

2.1 Model construction

The C-S-H model was constructed based on the tobermorite model with an interlamellar spacing of 11 Å, and followed the procedures proposed by Pellenq et al. (2009) and Abdolhosseini Qomi et al. (2014). Firstly, the tobermorite 11 Å without water treated with supercell and orthogonalization was taken as the initial configuration, and the structure size was 22.32 Å×22.17 Å×22.77 Å (L_x×L_y×L_z). Next, the silicate chains were broken by randomly removing some charge-neutral SiO_2 groups to match the experimental results obtained from nuclear magnetic resonance tests (Li J et al., 2019; Li B et al., 2020), thereby obtaining structures with different Ca/Si ratios (1.3, 1.7, and 1.9). Then, the water molecules were absorbed back into the dry structures above obtained from the previous step by grand canonical Monte Carlo (GCMC) method using CSHFF, and C-S-H molecular structures with different water contents (0%, 30%, 50%, 70%, and 100%) were obtained (Shahsavari et al., 2011). During the GCMC simulation, the chemical potential of the water was 0 eV, corresponding to the bulk water at room temperature. When the dry structures reached a saturated state, the water to silicon ratios were 1.02, 1.84, and 2.18 when the Ca/Si ratios were 1.3, 1.7, and 1.9, respectively, which were in accordance with those obtained from experiments (Allen et al., 2007). Then, a semi-classical MD simulation using ReaxFF potential with a time step of 0.25 fs was performed on the structures with adsorbed water molecules for 4 ns at room temperature, allowing water molecules to react with silica groups and interlayer calcium to form Si–OH and Ca–OH (Pitman and van Duin, 2012). The final equilibrated atomic configuration of C-S-H with a Ca/Si ratio of 1.7 is shown in Fig. 1.

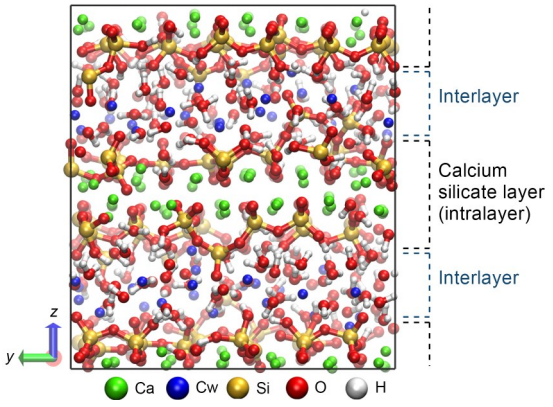

Fig. 1 Snapshot of the molecular model of C-S-H structure considered herein. Ca: intralayer calcium; Cw: interlayer calcium; Si: silicon; O: oxygen; H: hydrogen. References to color refer to the online version of this figure

2.2 Force field

CSHFF potential was used to simulate the interatomic interaction in the C-S-H system, except for the part handled by ReaxFF potential in the model building phase. By fitting ab initio-based lattice parameters and elastic constants of several minerals in cement-based materials, CSHFF potential has been widely and effectively used to predict the energy, structural information, and mechanical properties of cement-based materials, especially C-S-H. The force field parameters used in this simulation can be directly obtained

from the related references (Pitman and van Duin, 2012; Abdolhosseini Qomi et al., 2014). To confirm the reliability of the force field, results obtained by the MD simulation are usually compared with experimental and first-principle calculation results. In recent years, an alternative routine based on machine-learning interatomic potentials was proposed by Mortazavi et al. (2021a, 2021b), which had first-principle calculation accuracy but MD efficiency to predict the mechanical response of different materials. Their studies made a great contribution to bridging first-principle-based modes to continuum models, and provided a broad perspective for generating reliable potentials.

2.3 Simulation procedures

Firstly, to remove the internal stress for further structural and dynamic investigation, a supercell (2×2×2) of C-S-H molecular structure constructed above was equilibrated using CSHFF potential for 4 ns in an isothermal-isobaric (NPT) ensemble at 298 K and 101.325 kPa to removal internal stress for subsequent structural and dynamic analysis (Abdolhosseini Qomi et al., 2014). The size of the equilibrated structures was around 4.4 nm×4.4 nm×4.6 nm. Secondly, uniaxial tension tests were conducted on the different directions in the NPT ensemble with constant strain rate of 0.08 ps^{-1} to obtain the stress–strain relation of C-S-H. Then, shear loadings with a series of constant strain rates ranging from 0.8 to 0.0008 ps^{-1} in canonical (NVT) ensembles using the SLLOD method (Todd and Daivis, 2017) were conducted in the *xz* direction of C-S-H to clarify the effect of loading rate on the strength and stress relaxation of C-S-H.

To study the stress relaxation behavior of C-S-H subjected to different initial deformation states (shear, tensile, or compressive modes) with different deformation levels, different shear deformations (γ_{xz} and γ_{yz}) and uniaxial deformations (ε_x, ε_y, and ε_z) in opposite directions were applied individually to the equilibrated C-S-H structure. Four different initial shear deformations (shear angle γ=2°, 4°, 8°, and 12°) were selected to study the effect of different deformation magnitudes on the stress relaxation behavior. A uniaxial strain (ε=0.04) was used to study the effect of direction on the stress relaxation behavior of C-S-H.

To study the effect of the Ca/Si ratio on stress relaxation behavior, C-S-H with different Ca/Si ratios (1.3, 1.7, and 1.9) was firstly equilibrated for 4 ns in the NPT ensemble at 298 K and 101.325 kPa. Then, a shear deformation (γ_{xz}=4°), lower than the ultimate strain of the C-S-H molecular structure, was applied to the equilibrated C-S-H structure with different Ca/Si ratios. It was reported that the rupture strength of the C-S-H molecular structure was about 3 GPa by shear simulation (Pellenq et al., 2009). To study the effect of temperature on stress relaxation behavior, the C-S-H structure with a Ca/Si ratio of 1.7 was firstly heated from 298 to 373 or 423 K within 1 ns, and then allowed to relax in the NPT ensemble for 4 ns at the temperature to which it was heated. Secondly, the equilibrated C-S-H molecular structures were subjected to γ_{xz}=4° to investigate the stress relaxation behavior of C-S-H under different temperatures. When studying the effect of different water contents on the stress relaxation behavior of C-S-H molecular structure, the C-S-H model (Ca/Si ratio is 1.7) with different water contents (0%, 30%, 50%, 70%, and 100%) was equilibrated for 4 ns at 298 K and 101.325 kPa, prior to the application of γ_{xz}=4°.

In conventional stress relaxation experiments, the specimen is loaded to a specified strain at a constant strain loading rate under specified temperature or humidity conditions, and then the strain is sustained for a period of time. During the stress relaxation process, directions other than the strain direction are not constrained. To mimic the conventional stress relaxation experiments, the C-S-H structure was deformed to the desired shear deformation at a constant strain rate of 0.08 ps^{-1} in NVT using the SLLOD method for all the initial shear deformations mentioned above. For the uniaxial deformation, a constant strain rate of 0.08 ps^{-1} was used to make the C-S-H structure deform to the desired deformation in the NPT ensemble. Then, the C-S-H structure was maintained at the specific strain for 4 ns with a Nosé-Hoover thermostat and a time step of 1 fs. CSHFF potential was used throughout the equilibrated and stress relaxation processes. Periodic boundary conditions were applied in all directions. Additionally, the NPT ensemble was implemented to keep the pressure in those undeformed directions constant (101.325 kPa) during the stress relaxation process so that the effect of Poisson could be considered. All MD simulations in this study were performed using the Large-scale Atomic/Molecular Massively Parallel Simulator (LAMMPS) package.

3 Results and discussion

3.1 Stress relaxation of C-S-H

3.1.1 Effect of loading strain rate

To confirm the validity of the C-S-H model, we compared the mechanical parameters obtained in this study with those calculated from experiments and first-principles. In this study, several uniaxial tensile tests were performed on the C-S-H structure with a Ca/Si ratio of 1.7. Fig. 2 presents the stress–strain curves of C-S-H with a Ca/Si ratio of 1.7 under uniaxial tension tests, and Table 1 shows the related mechanical parameters obtained. In the *x*- and *y*-directions, Young's moduli in this simulation are in good agreement with those obtained from the nano-indentation tests (50–60 GPa), the ab initio calculation (55–68 GPa), and the MD simulation results (about 60 GPa) (Constantinides and Ulm, 2004, 2007; Pellenq et al., 2009; Hou et al., 2015b). The stress–strain curves in different directions can be divided into three stages: the elastic, yield, and damage stages (Fig. 2). In the elastic stage, the relation between stress and strain can be explained by Hooke's law. Note that the stress is lower in the *z*-direction than in the *x*- and *y*-directions, indicating that the mechanical performance of C-S-H in the *z*-direction is the weakest. In addition, the stress in the *z*-direction has a sudden drop at a strain of around 0.2 Å/Å, indicating the C-S-H structure suffers a brittle failure. The mechanical performance of C-S-H in this study was similar to that observed in other simulations (Hou et al., 2015b).

The effect of loading strain rate on the shear behavior of C-S-H in the *xz* direction with a Ca/Si ratio of 1.7 and subsequent stress relaxation results are presented in Fig. 3. The loading rate has an obvious impact on the evolution of the stress–strain curves and a positive relationship with the slope of stress–strain curves and strain at failure. When the strain rate is 0.08 ps^{-1}, the strain at failure is around γ_{xz}=8°. Additionally, the stress–strain curves under different strain

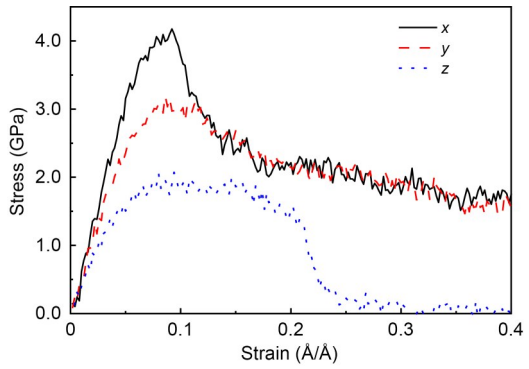

Fig. 2 Stress–strain curves of C-S-H with a Ca/Si ratio of 1.7 in different tensile loading directions

Table 1 Mechanical parameters of C-S-H with a Ca/Si ratio of 1.7 obtained from uniaxial tension tests

Direction	Young's modulus (GPa)	Yield strength (GPa)	Yield strain (Å/Å)
x	62	4.10	0.090
y	54	3.05	0.112
z	41	1.97	0.105

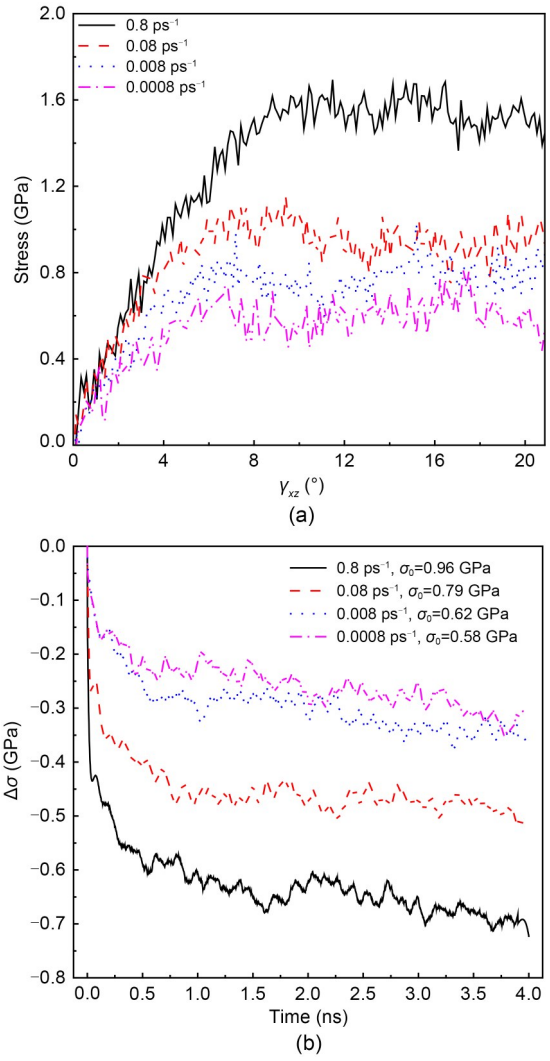

Fig. 3 Mechanical response of C-S-H with a Ca/Si ratio of 1.7 under different shear loading strain rates in the *xz* direction: (a) stress–strain curves; (b) evolution of the stress difference $\Delta\sigma$ in the stress relaxation process under γ_{xz}=4° (σ_0 is the initial stress)

rates have a similar shape and can also be divided into three stages: the elastic, yield, and plastic stages. As expected, a large stress can be obtained by a large loading strain rate. Similar results have been reported from tension tests on cementitious materials (Rossi, 1997). The results indicate that a small loading rate can provide sufficient time to allow the rearrangement of atoms or molecules, so as to enhance the growth of cracks in the C-S-H gel and lead to early failure. In addition, water confined in the interlayer region plays an important role in the return force and delays the failure of C-S-H. This effect becomes profound with the increase of loading strain rate (Hou et al., 2014b).

Under the same strain condition (γ_{xz}=4°), the effect of loading strain rate on the subsequent stress relaxation process is shown in Fig. 3b. Due to the existence of thermal fluctuations in the process of MD simulation, the stress relaxation results obtained from MD simulation are not constant. To demonstrate the effect of thermal fluctuations on the stress relaxation results, 10 stress relaxation tests were carried out. C-S-H with a Ca/Si ratio of 1.7 was first shear deformed to γ_{xz}=4° at a shear loading rate of 0.08 ps^{-1}, then a stress relaxation test with a length of 4 ns was performed. The stress relaxation result under this condition was used throughout this study. For each stress relaxation simulation, the stress value at specific time, such as at 0.5 ns, was obtained by averaging the stress data within 10 ps before and after this time so as to ensure the accuracy and rationality of stress data. Then, the stress data of 10 tests at a specific time were processed. Compared with the overall mean and standard deviation values at each specific time, the data used for figure rendering are reliable (Table 2).

It is clear from Fig. 3b that a large strain rate causes a large drop in stress in the early stage of the stress relaxation process, followed by a similar stress evolution stage. The stress difference $\Delta\sigma$ (calculated by Eq. (1)) is about 0.65 GPa at 1 ns when the applied strain rate is 0.8 ps^{-1}. When the strain rate is not larger than 0.008 ps^{-1}, this difference is not obvious. The effect of loading strain rate on the stress relaxation of C-S-H can be explained by the movement of water molecules confined in the interlayer region from the high-stress area to the low-stress area. The cracks expand further within a short time, resulting in rapid stress release in the early stage of the stress relaxation process.

Table 2 Mean and standard deviation values of the stress relaxation simulation results of C-S-H (Ca/Si ratio is 1.7, γ_{xz}=4°, and strain rate is 0.08 ps^{-1})

Time (ns)	Stress (GPa)		Standard deviation (%)
	Used in figures	Mean	
0.0	0.791	0.800	4.48
0.5	0.385	0.381	2.70
1.0	0.327	0.332	1.96
1.5	0.343	0.323	1.40
2.0	0.319	0.310	3.42
2.5	0.333	0.309	2.05
3.0	0.324	0.311	2.75
3.5	0.329	0.308	3.30
4.0	0.298	0.291	3.18

Considering the effect of water on the mechanical performance of the C-S-H gel, a loading strain rate of 0.08 ps^{-1} is adopted in the following sections. The size effect plays a critical role in the evaluation of fractures and stress condition, especially at nanoscale. Talebi et al. (2014) gave a unique insight into using reasonable model sizes in simulation. In the presence of cracks at nanoscale, they proposed the following relation as the fundamental assumption, based on homogenization theories. For the existence of disparate length scales, l_{Cr}=l_{RVE}=l_{Spec}, where l_{Cr}, l_{RVE}, and l_{Spec} are the sizes of the crack, respective volume element, and specimen, respectively. Because most of the tests performed in this study are within the elastic range, the size of the crack is much smaller than that of the model. Moreover, the use of period boundary conditions can mitigate the effect of size and improve the convergence of simulation results so as to ensure the accuracy of MD results.

3.1.2 Effect of initial deformation state

Different magnitudes of shear, tensile, or compressive deformation were applied to the equilibrated C-S-H system to reveal the stress relaxation behavior of C-S-H and its underlying mechanism. The stress evolution of C-S-H over time under different initial deformation states at a temperature of T=298 K with a Ca/Si ratio 1.7 is shown in Figs. 4 and 5. Whether C-S-H is subjected to a shear, tensile, or compressive deformation, the stress evolution of the entire C-S-H system takes on a typical L-shape during the stress relaxation process. As shown in Figs. 4a and 4b, in a certain range of shear deformation (γ_{xz} and γ_{yz}), the initial stress σ_0 increases with the increase of γ, indicating

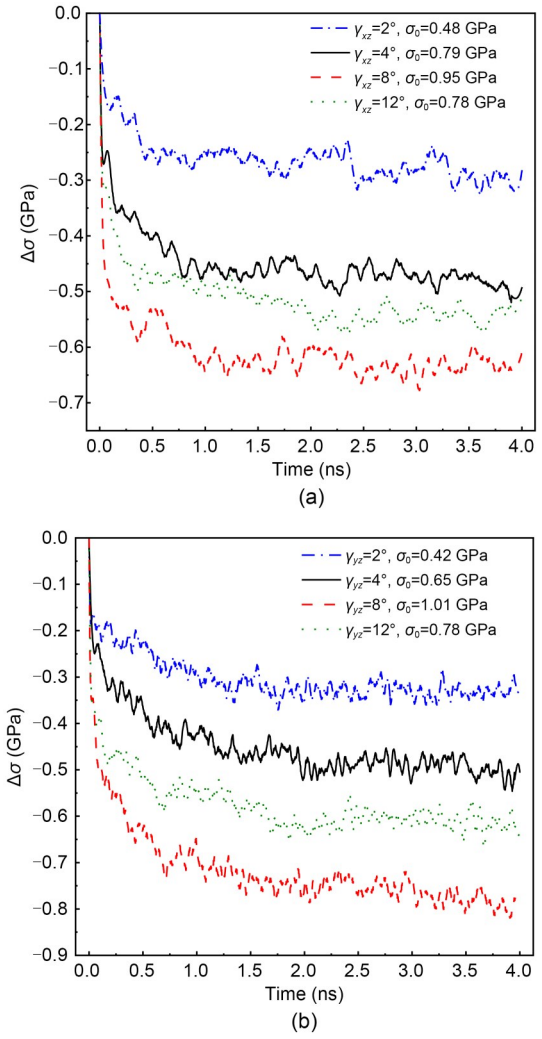

Fig. 4 Change in stress of C-S-H subjected to different shear deformations at T=298 K: (a) evolution of $\Delta\sigma$ under γ_{xz}; (b) evolution of $\Delta\sigma$ under γ_{yz}

that the applied shear deformations are in the elastic or elastoplastic range. As the relaxation time passes, the stress gradually decreases, and a high initial shear angle corresponds to a large stress difference $\Delta\sigma$:

$$\Delta\sigma=\sigma_t-\sigma_0, \tag{1}$$

where σ_t is the stress of C-S-H at time t. In addition, the stress declines slowly at a late stage. Such stress relaxation behavior under shear deformation is quite similar to that observed by experiment (Alizadeh et al., 2010). However, once the initial shear deformation exceeds the elastoplastic range, some micro cracks are probably generated within C-S-H systems, resulting in a relatively small $\Delta\sigma$ during the stress relaxation process. In addition, comparing Figs. 4a and 4b shows that the $\Delta\sigma$ of C-S-H under shear deformation γ_{yz} is slightly larger than that under shear deformation γ_{xz}, within the same relaxation time. For example, $\Delta\sigma$ under γ_{yz}=8° at 4 ns is about 0.78 GPa compared with 0.62 GPa under γ_{xz}=8°. This can be attributed to the structural heterogeneity caused by the orientation of the silicate chains in the calcium-silicate layer (Manzano et al., 2013). Figs. 5a and 5b show the stress evolution of the C-S-H system under tensile or compressive deformation ε=0.04 with different directions, respectively. Due to the structural heterogeneity of C-S-H, the stress behaviors in different directions also show some differences. As shown in Figs. 5a and 5b, the maximum σ_0 and residual stress are in the x-direction,

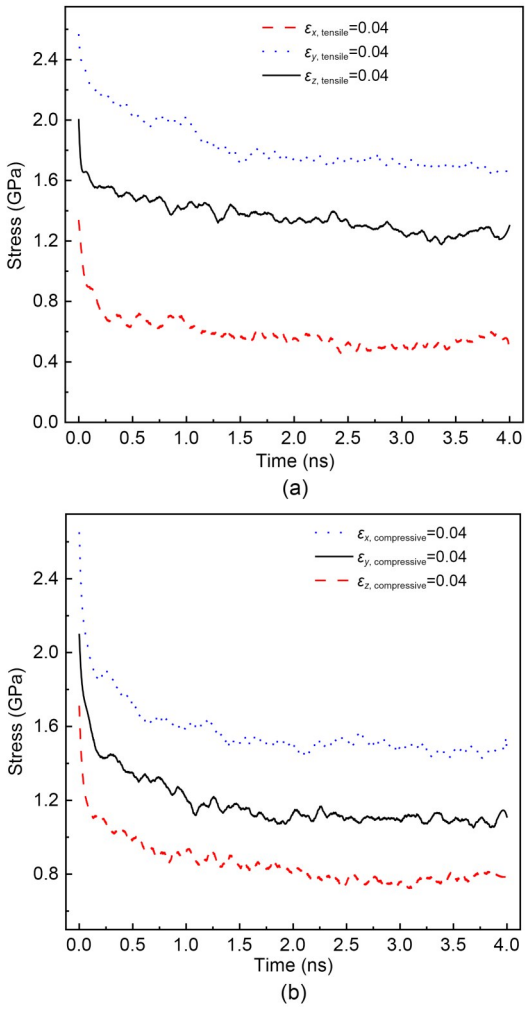

Fig. 5 Change in stress of C-S-H subjected to different uniaxial deformations at T=298 K: (a) evolution of stress under tensile deformation in different directions; (b) evolution of stress under compressive deformation in different directions

followed by those in the y-direction and z-direction. Comparing Figs. 5a and 5b shows that the $\Delta\sigma$ of the C-S-H system under compressive deformation is slightly larger than that under tensile deformation. For instance, $\Delta\sigma$ is 0.91 GPa when C-S-H is subjected to compressive deformation and 0.83 GPa when subjected to tensile deformation. However, regardless of whether the initial deformation is tensile or compressive, the residual stress in the x- or y-direction is similar, except in the z-direction. Compared to the other two directions, the z-direction is more prone to brittleness due to the unstable hydrogen bonding, which weakens the interlayer cohesion (Hou et al., 2015a, 2015b). Under the same initial deformation conditions, micro cracks are more likely to occur within the C-S-H during the stress relaxation process, especially in the interlayer region, resulting in increased stress relaxation and low residual stress (Beushausen et al., 2012; Giorla and Dunant, 2018).

To better understand why the stress relaxation of C-S-H occurs, atomic displacement magnitude profiles are shown in Fig. 6. Figs. 6a and 6b show C-S-H subjected to two shear deformations with γ=4°, while Figs. 6c and 6d show C-S-H subjected to tensile and compressive deformation, respectively, with strain ε=0.04. Comparing Figs. 1 and 6 shows that whether the C-S-H is subjected to shear, tensile, or compressive deformation, the highlighted region in the C-S-H structure is concentrated mainly in the interlayer region composed of water molecules, hydroxyl groups, as well as interlayer calcium atoms. The dark blue region is referred to as the intralayer region where calcium-silicate layers exist. The stress relaxation of C-S-H is attributed mainly to atomic movement within the interlayer region.

To regain the equilibrium state, the movement of interlayer atoms causes some chemical events to occur in the interlayer region of C-S-H, especially the

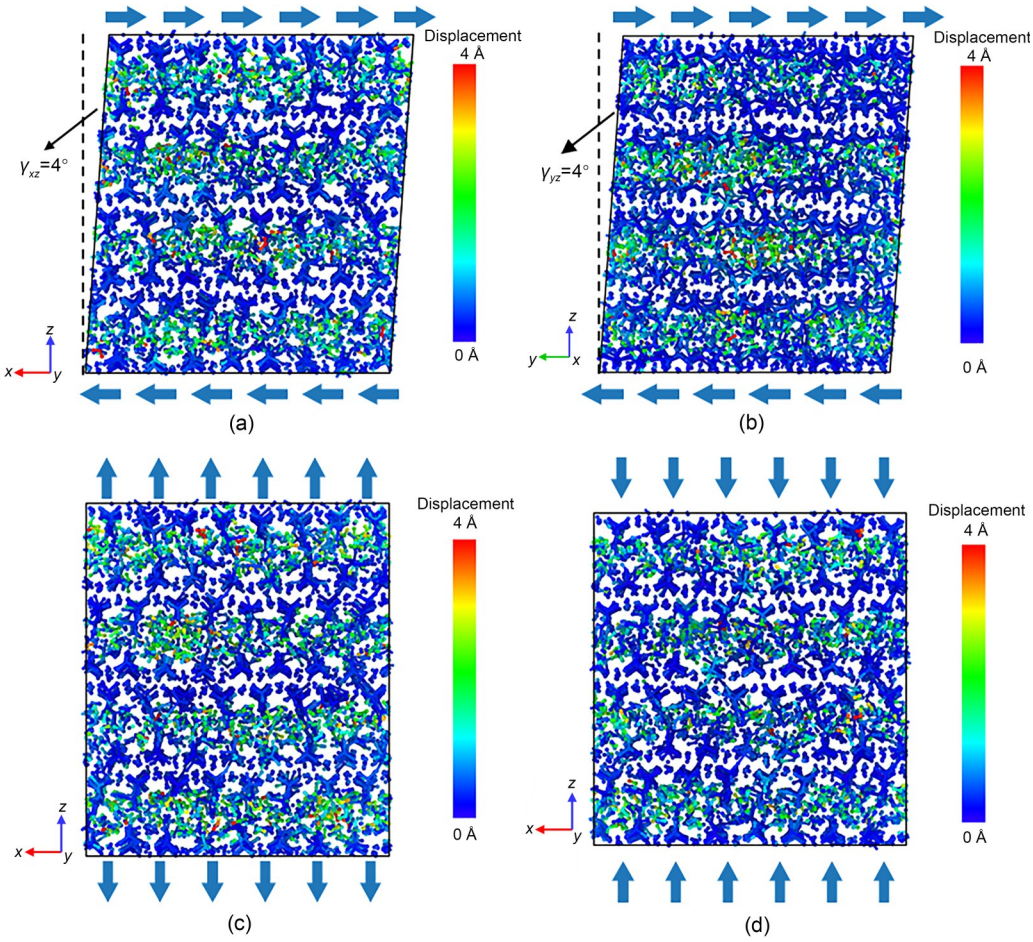

Fig. 6 Magnitude of the atomic displacement of the C-S-H structure under different initial deformation states: (a) γ_{xz}=4°; (b) γ_{yz}=4°; (c) $\varepsilon_{tensile}$=0.04; (d) $\varepsilon_{compressive}$=0.04. References to color refer to the online version of this figure

breakage and reformation of bonds, which is similar to what occurs during the process of creep. There are two main bonds associated with the process of stress relaxation: the Ca–O ionic bond and the hydrogen bond (H-bond). According to previous studies (Wang et al., 2004; Hou et al., 2014a), a Ca–O ionic bond is formed when the distance between the calcium and oxygen atoms is not larger than 3 Å. Two conditions are required for the formation of an H-bond: the first is that the distance between the donor hydrogen atom and the acceptor oxygen atom is not larger than 2.45 Å, and the second is that the angle between the donor oxygen-donor hydrogen vector and the donor oxygen-acceptor oxygen vector is not larger 30°. To evaluate the influence of initial deformation levels on the stress relaxation process of the C-S-H structure, the history-dependent $C(t)$ associated with the fluctuation of the bonds in the interlayer region is calculated (Youssef et al., 2011; Gowers and Carbone, 2015):

$$C(t)=\frac{\langle \delta h(t)\,\delta h(0)\rangle}{\langle \delta h(0)\,\delta h(0)\rangle}, \tag{2}$$

where $\delta h(t)=h(t)-\langle h\rangle$, $h(t)$ is a binary operator between two bonded atoms that takes a value of one if a pair is bonded and zero if not, and $\langle h\rangle$ is the average of the binary operator over all pairs and times. Given that the pairs are intact at time 0, it can reflect the probability whether a pair exists at time t as well as the lifetime of the pairs. Therefore, it can also to some extent reflect the rate of bond breakage. The $C(t)$ values of the interlayer Ca–O bonds and H-bonds under different γ_{xz} and γ_{yz} at T=298 K are shown in Fig. 7. Both $C(t)$ decay at a rapid rate in the initial stage of stress relaxation, then the rate of decay gradually decreases with time, which is consistent with the evolution of stress presented in Figs. 4a and 4b. Also, the rate of breakage of the interlayer Ca–O bonds and H-bonds is rapid at the beginning and decreases with

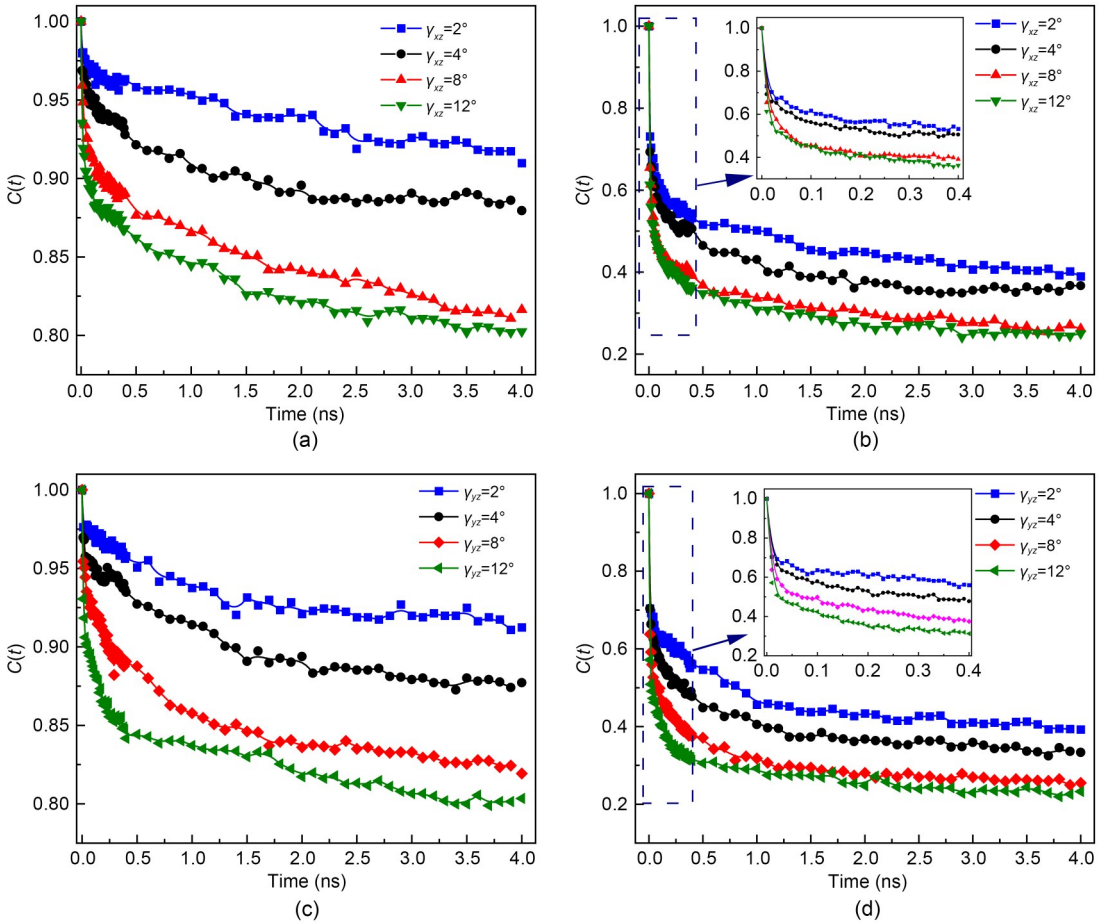

Fig. 7 $C(t)$ of the interlayer Ca–O bonds and H-bonds under different shear states: (a) $C(t)$ of interlayer Ca–O bonds under γ_{xz}; (b) $C(t)$ of H-bonds under γ_{xz}; (c) $C(t)$ of interlayer Ca–O bonds under γ_{yz}; (d) $C(t)$ of H-bonds under γ_{yz}

time. The changes in the local structure over time during the stress relaxation process are shown in Fig. 8. As expected, to achieve a relatively low energy state, the positions of interlayer calcium atoms, hydroxyl groups, and water molecules in the interlayer region are constantly changing, accompanied by the breakage and reformation of the Ca–O ionic bonds and H-bonds. In addition, as the initial deformation increases, the $C(t)$ values of the interlayer Ca–O ionic bonds and H-bonds decrease. For example, when $\gamma_{xz}=2°$, these two values are 0.91 and 0.40, respectively; when $\gamma_{xz}=12°$, they become 0.80 and 0.25. The relationship between the $C(t)$ of the interlayer Ca–O bonds and H-bonds and the initial shear deformation indicates that the large initial deformation is in accord with the high rate of breakage of the interlayer Ca–O bonds and H-bonds in the initial stage. Comparing the $C(t)$ values of the interlayer Ca–O bonds and H-bonds shows that the $C(t)$ value of the interlayer Ca–O bonds is larger than that of the H-bonds under the same shear deformation. It can be inferred that in the stress relaxation process of the C-S-H structure, the breakage and reformation of H-bonds related to the rearrangement of hydroxyl groups and water molecules account for the dominating cause, while the breakage and reformation of the interlayer Ca–O bonds are a secondary cause.

To better understand the process of stress relaxation of the C-S-H structure, the potential energy of C-S-H systems subjected to γ_{xz} and γ_{yz} of different initial magnitudes is shown in Fig. 9. The stress relaxation

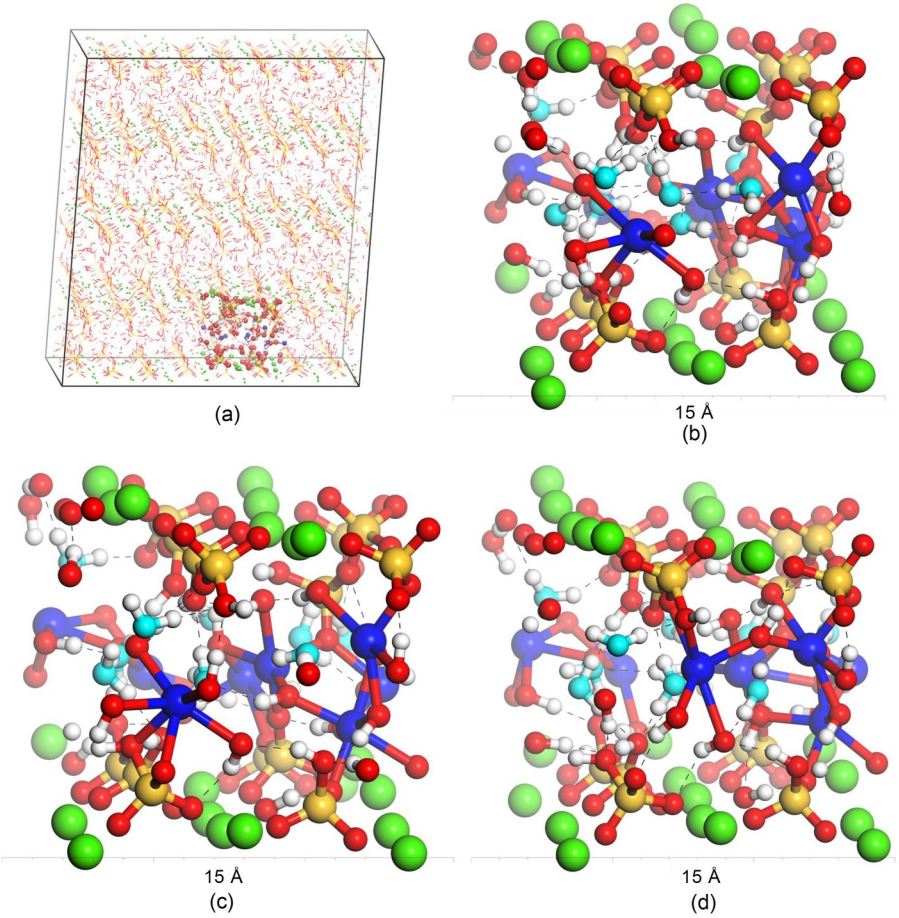

Fig. 8 Changes in local microstructure during the stress relaxation process at different time nodes with the breakage and reformation of interlayer Ca–O bonds and H-bonds: (a) molecular structure of C-S-H under $\gamma_{xz}=4°$, $T=298$ K, and $t=0$ ps (the local structure shown in ball-and-stick is the chosen region); (b) local molecular structure at $t=100$ ps (the dashed black line indicates the H-bonds); (c) local molecular structure at $t=200$ ps; (d) local molecular structure at $t=4$ ns. The Ca–O bonds and H-bonds defined herein refer to the criterion proposed by Hou et al. (2014a) and Wang et al. (2004), respectively. The atoms shown here are consistent with those shown in Fig. 1 except that cyan means oxygen in water molecules. References to color refer to the online version of this figure

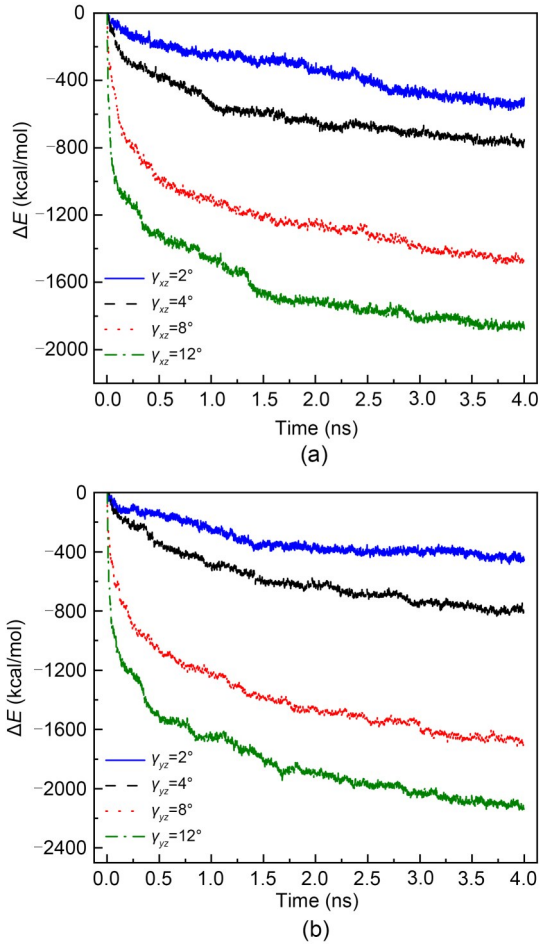

Fig. 9 Evolution of Δ*E* during the stress relaxation process subjected to two shear deformation states at *T*=298 K: (a) γ_{xz}; (b) γ_{yz}

process is accompanied by a decline in potential energy regardless of the magnitude and direction of the initial shear deformation. Additionally, the magnitude of initial shear deformation and the difference in potential energy (Δ*E*), calculated by Eq. (3), have a positive relation.

$$\Delta E = E_t - E_0, \tag{3}$$

where E_t and E_0 are the potential energies of the C-S-H system at time t and 0, respectively. For instance, Δ*E* is −504 kcal/mol when γ_{xz}=2° and −1875 kcal/mol when γ_{xz}=12° (1 kcal=4184 J). According to previous research (Morshedifard et al., 2018), C-S-H can be regarded as a kind of metastable material: the lower the energy state to which C-S-H relaxes, the higher the energy barriers to further relaxation. That could explain why the stress, the $C(t)$ of the interlayer Ca–O bonds and H-bonds, and the potential energy of the C-S-H system decrease at a high rate in the initial stage of the stress relaxation process and then gradually over time. In addition, since the initial shear deformation is applied to C-S-H almost immediately as an external energy source, the larger the initial shear deformation applied to C-S-H, the more external energy C-S-H obtains and the more unstable the C-S-H system becomes. The underlying mechanism can be explained by the large initial deformation leading to considerable losses of potential energy and stress in the elastic/elastoplastic strain range. These findings are broadly consistent with those from the activation exergy theory (Venkovic et al., 2014).

3.2 Effect of Ca/Si ratio and temperature

The chemistry, nanostructure, and morphology of C-S-H are affected by the Ca/Si ratio and temperature, further affecting its mechanical properties (Gallucci et al., 2013; Cuesta et al., 2021; Zheng et al., 2021; Wang et al., 2022). To reveal the effect of Ca/Si ratio and temperature on the stress relaxation and their underlying mechanisms, the stress relaxation of C-S-H with different Ca/Si ratios and subjected to different temperatures was investigated. As shown in Fig. 10a, with increasing Ca/Si ratio, both σ_0 and the residual stress of the C-S-H structure decrease during the stress relaxation process. When the Ca/Si ratio is 1.3, σ_0 is 0.88 GPa and the residual stress at 4 ns is 0.45 GPa, while when Ca/Si ratio is 1.9, they are 0.70 and 0.17 GPa, respectively. Increasing the Ca/Si ratio of C-S-H leads to a weakening of the interaction between the interlayer calcium and calcium-silicate layers, resulting in a decline in interlayer cohesion (Masoumi et al., 2019). Fig. 10b shows that at high temperature the stress decreases fast and has a low value. For the same shear deformation at 4 ns, the stress decreases from 0.30 GPa at 298 K to 0.07 GPa at 423 K. This is similar to the experimental results obtained by Wang et al. (2015) which showed that an increase in temperature led to an increase in the stress relaxation and a decrease in residual stress in cement clinkers. In terms of activation energy theory, the temperature serves as an external energy source to provide additional energy to the C-S-H system. High temperature provides sufficient energy for the C-S-H system to easily overcome the energy barrier, so that a low energy state can be achieved. In addition, in some specific hydrothermal

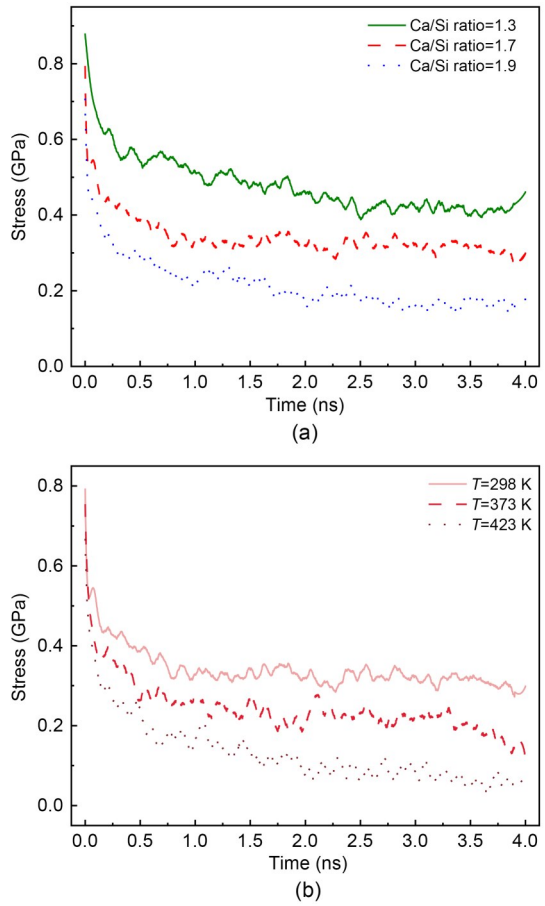

Fig. 10 Change in stress of C-S-H subjected to different Ca/Si ratios and temperatures under γ_{xz}=4°: (a) evolution of stress with different Ca/Si ratios at T=298 K; (b) evolution of stress at different temperatures with a Ca/Si ratio of 1.7

conditions, the amorphous C-S-H can easily transform into well-defined crystalline phases, such as α-dicalcium silicate hydrate, giving C-S-H poor mechanical performance (Tian et al., 2021). These effects explain why high temperature results in a low stress level.

To further understand the mechanisms of the effects of Ca/Si ratio and temperature on the stress relaxation behavior of C-S-H, the viscosity of the interlayer region was considered. At the microscopic level, viscosity can be regarded as the internal friction among molecules as they move under external forces, which are determined mainly by the intermolecular interactions and temperature (Han et al., 2010; Feng et al., 2018). MSD enables changes in the viscosity of the interlayer region of C-S-H during the stress relaxation process to be considered (Tang and Wong, 2015). The magnitude of atomic movement in the interlayer region was evaluated by MSD (Youssef et al., 2011):

$$d_{\mathrm{ms}}(t)=\langle\Delta r^2(t)\rangle=\left\langle\frac{1}{N}\sum_{i=1}^{N}\left|r_i(t)-r_i(0)\right|^2\right\rangle, \quad (4)$$

where $d_{\mathrm{ms}}(t)$ is the MSD at time t, N is the number of atoms to be averaged, and $r_i(t)$ and $r_i(0)$ are the coordinates of the ith atom at time t and 0, respectively. The angular brackets represent an average of the particles. The MSD of each atom in C-S-H during the stress relaxation process at different Ca/Si ratios and temperatures is shown in Fig. 11. From Fig. 11a, atoms in the interlayer region have fast dynamics, while those in the calcium-silicate layers show slow movement, confirming that the stress relaxation of C-S-H can again be attributed mainly to atomic movement in the interlayer region. In the interlayer region, water molecules have the fastest dynamics, and interlayer calcium has the slowest, as verified by the $C(t)$ values of the interlayer Ca–O bonds and H-bonds (Fig. 12). As shown in Figs. 11b–11d, both a large Ca/Si ratio and a high temperature have an accelerating effect on the dynamics of atoms in the interlayer region that promotes stress relaxation. However, their underlying mechanisms have some differences. In the interlayer region, water molecules are confined by the network formed by the stable H-bonds associated with the Ca–OH and Si–OH, as well as the ionic bonds formed by the interaction between the solvated interlayer Ca atoms and defective silicate chains (Hou et al., 2015c). A high temperature provides sufficient external energy to allow the atoms to have a high velocity and easily overcome the energy barriers. Meanwhile, drastic bond breakage and reformation occur, represented by the $C(t)$ of the interlayer Ca–O bonds and H-bonds (Fig. 12). A large Ca/Si ratio leads to many defects in the silicate chains that are filled with water molecules, weakening the constraint of the network and giving C-S-H an amorphous structure (Hou et al., 2014a; Masoumi et al., 2019). However, with regard to the given ranges of Ca/Si ratio and temperature in this study, it seems that the effect of the Ca/Si ratio is not as profound as that of temperature. When the Ca/Si ratio of C-S-H reaches a certain value, the constraining effect of the network on the movement of water molecules is almost unchanged. Thus, the MSD of water molecules and the $C(t)$ of H-bonds in C-S-H with a Ca/Si ratio of 1.7 or 1.9 are almost the same in the late stage.

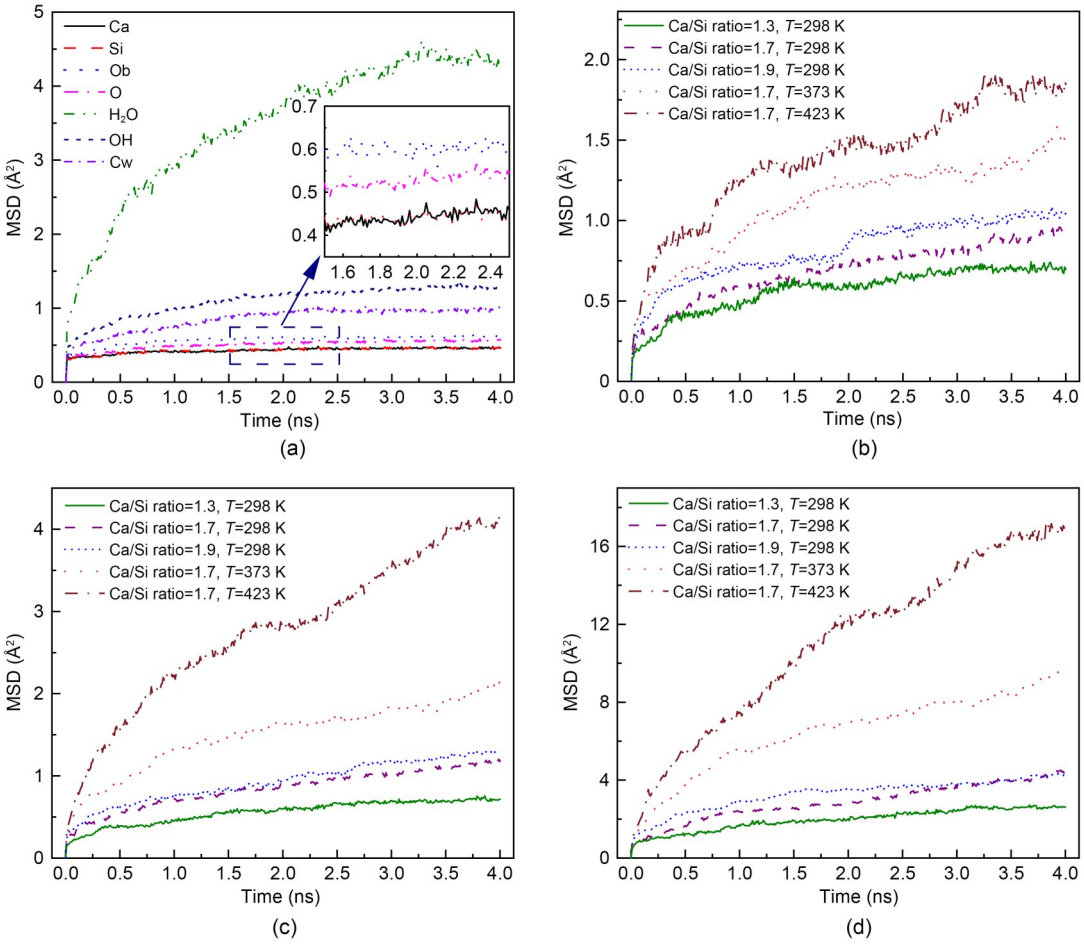

Fig. 11 MSD of constituent parts in the C-S-H system under γ_{xz}=4°: (a) MSD of each atom/molecule/group in C-S-H at T= 298 K (Ob: bridge oxygen atom); (b) MSD of interlayer calcium; (c) MSD of hydroxyl group; (d) MSD of water molecule

3.3 Effect of water content

To reveal the effect of water content on the stress relaxation behavior of C-S-H, the evolution of $\Delta\sigma$ (calculated by Eq. (1)) of C-S-H with 0%, 30%, 50%, 70%, and 100% water content were studied under γ_{xz}= 4° at T=298 K (Fig. 13). When there are no water molecules in the C-S-H, the stress inside C-S-H drops twice during the stress relaxation process: once in the first stage, by 0.52 GPa, and once again at 1.7 ns, by 0.27 GPa. The stress evolution of the C-S-H is changed after 30% water is added to the dry structure, reflected mainly in the first stage. The stress reduction is larger than that in the dry condition, while the final residual stress is basically the same as that in the dry condition. When the water content of the C-S-H structure increases to 50%, the stress relaxation of C-S-H becomes easier, and the secondary stress reduction that occurs in the cases of 30% water content and a dry state does not take place. However, when the water content exceeds 50%, $\Delta\sigma$ decreases with additional water absorbed. These results of stress evolution during the stress relaxation process are similar to those obtained by Liang et al. (2022) for the stress relaxation of C-S-H colloid at different humidities. In addition, the stress evolution of the C-S-H is seriously affected by the interlayer water content, which is in agreement with the findings of Alizadeh et al. (2010). They proposed a model for stress relaxation and creep by studying the viscoelastic nature of glass, C-S-H, and cement paste. This model indicated that the removal of a certain amount of water would increase the stress relaxation of C-S-H, and that some inconsistent changes in the stress relaxation after interlayer water removal may be due to the cross-linking of silicate tetrahedra and the interaction of calcium ions with silicate chains at different humidity levels.

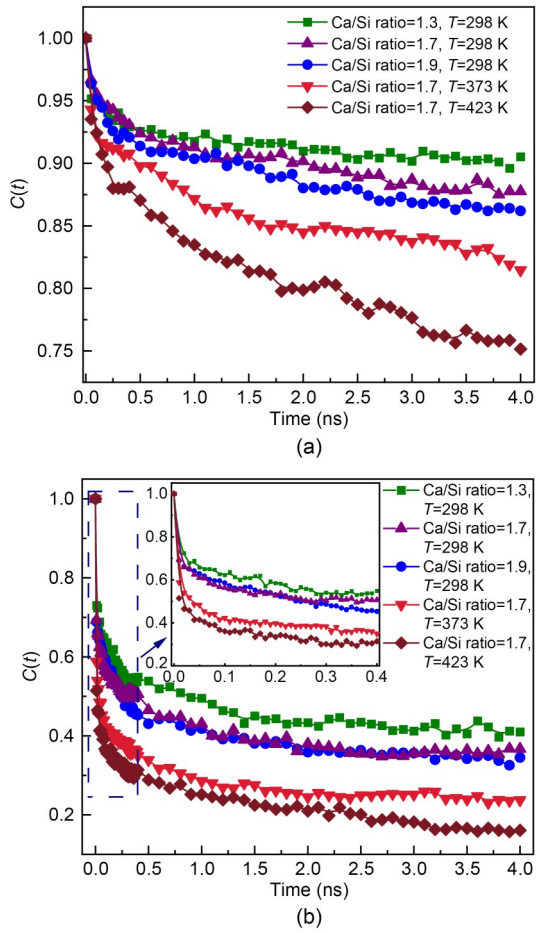

Fig. 12 $C(t)$ of the interlayer Ca–O bonds (a) and H-bonds (b) subjected to different Ca/Si ratios and temperatures under γ_{xz}=4°

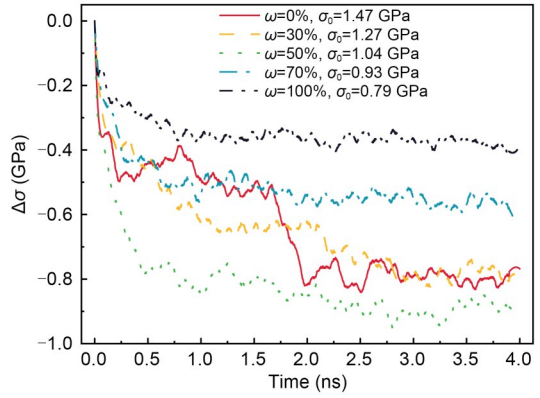

Fig. 13 Evolution of $\Delta\sigma$ of C-S-H with different water contents (ω) under γ_{xz}=4° and T=298 K

A structural analysis was performed to reveal the structural transformation of C-S-H with the removal of water. The atomic number density profiles along the z-direction for the intralayer atoms and interlayer atoms in four equilibrated atoms with different water contents as a function of the distance along the z-direction are shown in Fig. 14. They show that the water content plays a quite important role in the distribution of interlayer atoms. As water molecules are removed from the interlayer region, the interlayer spacing decreases. However, the intralayer spacing is hardly affected by the water content and remains unchanged. Obviously, the cohesion between the calcium-silicate layer and the interlayer region is significantly affected by the interlayer water. The results also suggest that the removal of interlayer water molecules may enhance the probability of interaction between the silicate tetrahedron and the interlayer calcium (Alizadeh et al., 2010). As the water content declines, the number of interlayer Ca–O bonds increases while the number of H-bonds apparently decreases. In such case, the packing of water molecules transforms from a multilayer to a monolayer configuration, leading to the evolution of the H-bond type, in turn affecting the bridging between nearby calcium-silicate layers (Hou et al., 2014a). Therefore, interactions between the interlayer atoms and the calcium-silicate layer atoms are responsible for the stress relaxation of C-S-H at different humidity levels.

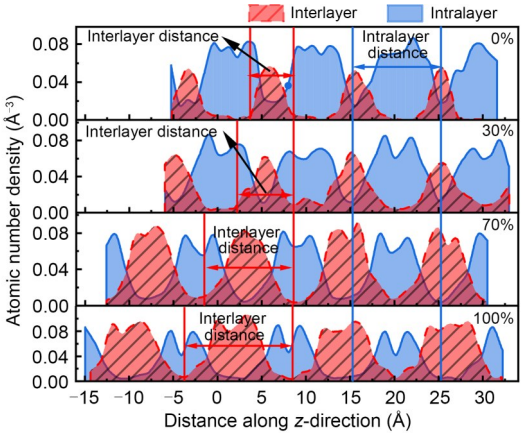

Fig. 14 Atomic number density profiles of interlayer and intralayer atoms in equilibrated C-S-H along the z-direction with water contents of 0%, 30%, 70%, and 100% from top to bottom

During the stress relaxation process, plastic deformation increases continuously. To evaluate the stress relaxation behavior of C-S-H with different water contents, the local deformation events must be identified. Falk and Langer (1998) introduced the $D^2_{\min}$ measure for identifying the nonaffine component of the local

deformation of an atomic system within a cutoff of r_{cut}. The idea is to map all bonds between the ith atom and neighboring atoms during the time interval Δt using an affine deformation with best-fit local transformation matrix $\boldsymbol{J}_i$. D^2_{min} is the mean squared residual of this fit (Shimizu et al., 2007; Priezjev, 2017). Then, the nonaffine component of local deformation is measured by

$$D^2_{min}=\frac{1}{N_i}\sum_{j=1}^{N_i}\left\{r_j(t)-r_i(t)-\boldsymbol{J}_i\left[r_j(t-\Delta t)-r_i(t-\Delta t)\right]\right\}^2, \tag{5}$$

where $r_i(t)$ is the position of the ith atom at time t and N_i is the sum of nearest-neighbor atoms within r_{cut} from $r_i(t)$. The value of D^2_{min}, the local deviation from affine deformation during the time interval $[t-\Delta t, t]$, can also be used to identify shear transformation zones and shear bands (Jana and Pastewka, 2019). Fig. 15 contains six different plots of D^2_{min} for C-S-H, all subjected to γ_{xz}=4°, here calculated for a cutoff r_{cut}= 3 Å. Fig. 15a shows the plots of D^2_{min} for the C-S-H structure without water. Due to the absence of water molecules, the C-S-H structure is amorphous and the cohesion between the calcium-silicate layers depends on the ionic bond formed by the interlayer calcium and oxygen in the calcium-silicate layer. The nonaffine deformation occurs as a longitudinal shear band in the middle of the C-S-H structure, accompanied by some small isolated events. Later, a transverse shear band is formed by a series of small nonaffine deformations in close proximity (Fig. 15b). The development of nonaffine deformations is responsible for the decline in secondary stress during the stress relaxation process. When the water content of C-S-H increases to 30%, the C-S-H structure is somewhat layered, and the water molecules are presented mainly in the form of bound water (Si–OH and Ca–OH), making the C-S-H structure dense. In addition, the remaining free water acts as a lubricant, alleviating the decline in secondary stress in the stress relaxation process. As shown in Fig. 15c, the longitudinal shear band appears to be weakened by the transverse shear band mainly located in the interlayer region. When the water content of the C-S-H structure reaches 50%, the layered structure of C-S-H becomes distinct. Considering that the monolayer water molecules formed in the interlayer region significantly promote the slip of the calcium-silicate layer and the deformation of the C-S-H structure, the stress relaxation of C-S-H becomes easy. Transverse shear bands, located in the interlayer region, gradually dominate the stress relaxation process (Fig. 15d). In addition, some nonaffine deformation still occurs

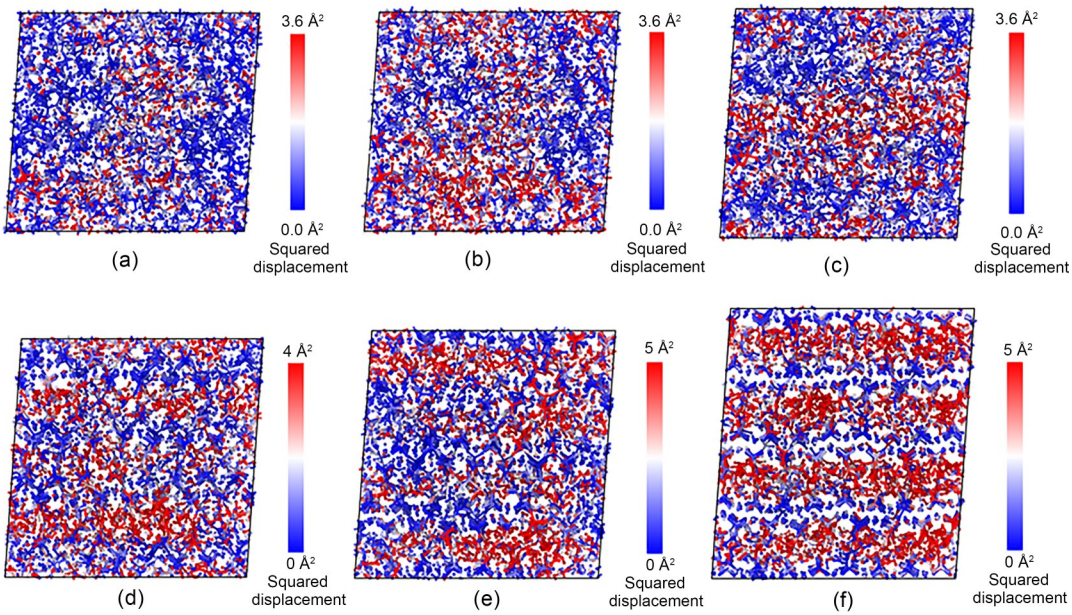

Fig. 15 Intensity plots of nonaffine squared displacement of C-S-H system with different water contents (r_{cut}=3 Å): (a) ω=0%, t=300 ps, Δt=300 ps; (b) ω=0%, t=2.5 ns, Δt=2.5 ns; (c) ω=30%, t=300 ps, Δt=300 ps; (d) ω=50%, t=300 ps, Δt=300 ps; (e) ω=70%, t=300 ps, Δt=300 ps; (f) ω=100%, t=300 ps, Δt=300 ps

in the calcium-silicate layers, forming a longitudinal shear band with some of the nonaffine deformations occurring in the interlayer region. As more water molecules are added to the C-S-H structure (Figs. 15e and 15f), few nonaffine deformations occur in the calcium-silicate layers, and the role of interlayer atomic movement in the stress relaxation process becomes increasingly important.

The effect of water molecules on the process of stress relaxation of C-S-H can be explained as follows. When the water content of C-S-H is lower than 50%, water has a prominent influence on the morphology of C-S-H. As the water content increases, the C-S-H structure transforms from a relatively disordered structure to a clearly layered one, remarkably affecting the stress relaxation behavior of C-S-H. However, when the water content is higher than 50%, the increasing water molecules lead to a weakening of the bonds between the calcium-silicate layers causing them to "slip" easily, thereby reducing the stress relaxation occurring in C-S-H as the water content increases.

4 Conclusions

The effects of different initial deformation states, Ca/Si ratios, temperatures, and water contents on the stress relaxation behavior of C-S-H, as well as the underlying stress relaxation mechanisms at the atomic-level, were studied using MD simulation with a CSHFF. The results of our simulations were in good agreement with those published from experiments. The simulations explained the stress relaxation characteristics at the atomic level and bridged the gap between atomic simulation and experimentation. The following findings were obtained:

1. The stress relaxation response of C-S-H occurs regardless of whether it is under initial shear, tensile, or compressive deformation, and shows a heterogeneous characteristic. The evolution of stress during the stress relaxation process originates mainly from the breakage and reformation of the H-bond and Ca–O bond network in the interlayer region, accompanied by the reduction of potential energy, thus reaching a relatively low energy state. A large initial deformation results in a short interlayer Ca–O and H-bond lifetime and a large drop in potential energy.

2. A large Ca/Si ratio or high temperature leads to low viscosity in the interlayer region and low cohesion between the calcium-silicate layer and the interlayer region, resulting in high atomic dynamics, especially for water molecules, hydroxyl groups, and interlayer calcium atoms. The initial stress and residual stress of C-S-H in the stress relaxation process decrease as the Ca/Si ratio or temperature increases.

3. Water molecules play a critical role in the stress relaxation performance of C-S-H. When the water content of C-S-H decreases from saturation state to 50%, the morphology of interlayer water molecules gradually transforms from a multi-layer to a monolayer configuration. Nonaffine deformation occurs mainly in the interlayer region, but gradually increases in the calcium-silicate layers, and the stress relaxation process of C-S-H also gradually speeds up. As more and more water molecules are removed from the interlayer region, a longitudinal shear band gradually replaces the transverse band in the nonaffine deformation, and the stress relaxation process of C-S-H gradually slows down. In addition, when the water content of C-S-H lowers to a certain extent, some small adjacent nonaffine deformations connect with each other to form a transverse shear band when the stress relaxation time is long. This accounts for the secondary stress drop in the stress relaxation process.

Acknowledgments

This work is supported by the National Natural Science Foundation of China (Nos. 51602229 and U2040222), the Opening Project of Key Laboratory of Advanced Civil Engineering Materials of Ministry of Education (Tongji University), and the Water Conservancy Science and Technology Project of Hunan Province (No. XSKJ2021000-15), China.

Author contributions

Zhicheng GENG: investigation, methodology, data curation, formal analysis, visualization, writing–original draft. Shengwen TANG: conceptualization, funding acquisition, supervision, validation, writing–review & editing. Yang WANG: visualization, formal analysis, project administration. Hubao A: validation, writing–review & editing. Zhen HE: resources, methodology. Kai WU: supervision, data curation. Lei WANG: writing–review & editing.

Conflict of interest

Zhicheng GENG, Shengwen TANG, Yang WANG, Hubao A, Zhen HE, Kai WU, and Lei WANG declare that they have no conflict of interest.

References

Abdolhosseini Qomi MJ, Krakowiak KJ, Bauchy M, et al., 2014. Combinatorial molecular optimization of cement hydrates. *Nature Communications*, 5:4960. https://doi.org/10.1038/ncomms5960

Alizadeh R, Beaudoin JJ, Raki L, 2010. Viscoelastic nature of calcium silicate hydrate. *Cement and Concrete Composites*, 32(5):369-376. https://doi.org/10.1016/j.cemconcomp.2010.02.008

Allen AJ, Thomas JJ, Jennings HM, 2007. Composition and density of nanoscale calcium–silicate–hydrate in cement. *Nature Materials*, 6(4):311-316. https://doi.org/10.1038/nmat1871

Arayro J, Dufresne A, Zhou TT, et al., 2018. Thermodynamics, kinetics, and mechanics of cesium sorption in cement paste: a multiscale assessment. *Physical Review Materials*, 2(5):053608. https://doi.org/10.1103/PhysRevMaterials.2.053608

Atutis M, Valivonis J, Atutis E, 2018. Experimental study of concrete beams prestressed with basalt fiber reinforced polymers. Part II: stress relaxation phenomenon. *Composite Structures*, 202:344-354. https://doi.org/10.1016/j.compstruct.2018.01.109

Bazant ZP, Chern JC, 1985. Concrete creep at variable humidity: constitutive law and mechanism. *Materials and Structures*, 18(1):1-20. https://doi.org/10.1007/BF02473360

Bažant ZP, Hauggaard AB, Baweja S, et al., 1997. Microprestress-solidification theory for concrete creep. I: aging and drying effects. *Journal of Engineering Mechanics*, 123(11):1188-1194. https://doi.org/10.1061/(asce)0733-9399(1997)123:11(1188)

Beushausen H, Masuku C, Moyo P, 2012. Relaxation characteristics of cement mortar subjected to tensile strain. *Materials and Structures*, 45(8):1181-1188. https://doi.org/10.1617/s11527-012-9825-2

Brooks JJ, Neville AM, 1976. Relaxation of stress in concrete and its relation to creep. *Journal Proceedings*, 73(4):227-232. https://doi.org/10.14359/11070

Chen J, Fang L, Chen HQ, et al., 2022. The loading speed facilitating stress relaxation behaviors of surface-modified silicon: a molecular dynamics study. *Journal of Molecular Modeling*, 28(6):160. https://doi.org/10.1007/s00894-022-05136-5

Chen JK, Qian C, 2017. Loading history dependence of retardation time of calcium-silicate-hydrate. *Construction and Building Materials*, 147:558-565. https://doi.org/10.1016/j.conbuildmat.2017.04.183

Ciarella S, Sciortino F, Ellenbroek WG, 2018. Dynamics of vitrimers: defects as a highway to stress relaxation. *Physical Review Letters*, 121(5):058003. https://doi.org/10.1103/PhysRevLett.121.058003

Constantinides G, Ulm FJ, 2004. The effect of two types of C-S-H on the elasticity of cement-based materials: results from nanoindentation and micromechanical modeling. *Cement and Concrete Research*, 34(1):67-80. https://doi.org/10.1016/S0008-8846(03)00230-8

Constantinides G, Ulm FJ, 2007. The nanogranular nature of C-S-H. *Journal of the Mechanics and Physics of Solids*, 55(1):64-90. https://doi.org/10.1016/j.jmps.2006.06.003

Cuesta A, Santacruz I, de la Torre AG, et al., 2021. Local structure and Ca/Si ratio in C-S-H gels from hydration of blends of tricalcium silicate and silica fume. *Cement and Concrete Research*, 143:106405. https://doi.org/10.1016/j.cemconres.2021.106405

Cygan RT, Liang JJ, Kalinichev AG, 2004. Molecular models of hydroxide, oxyhydroxide, and clay phases and the development of a general force field. *The Journal of Physical Chemistry B*, 108(4):1255-1266. https://doi.org/10.1021/jp0363287

Ding H, Chen JK, 2019. Research on the resistivity attenuation law of cementitious conductive composites induced by stress relaxation. *Construction and Building Materials*, 206:347-354. https://doi.org/10.1016/j.conbuildmat.2019.02.075

Du HJ, Pang SD, 2021. Long-term influence of nanosilica on the microstructures, strength, and durability of high-volume fly ash mortar. *Journal of Materials in Civil Engineering*, 33(8):04021185. https://doi.org/10.1061/(asce)mt.1943-5533.0003822

Falk ML, Langer JS, 1998. Dynamics of viscoplastic deformation in amorphous solids. *Physical Review E*, 57(6):7192-7205. https://doi.org/10.1103/PhysRevE.57.7192

Fang GH, Zhang MZ, 2020. Multiscale micromechanical analysis of alkali-activated fly ash-slag paste. *Cement and Concrete Research*, 135:106141. https://doi.org/10.1016/j.cemconres.2020.106141

Feldman RF, 1972. Mechanism of creep of hydrated Portland cement paste. *Cement and Concrete Research*, 2(5):521-540. https://doi.org/10.1016/0008-8846(72)90107-X

Feng D, Li XF, Wang XZ, et al., 2018. Capillary filling under nanoconfinement: the relationship between effective viscosity and water-wall interactions. *International Journal of Heat and Mass Transfer*, 118:900-910. https://doi.org/10.1016/j.ijheatmasstransfer.2017.11.049

Frech-Baronet J, Sorelli L, Charron JP, 2017. New evidences on the effect of the internal relative humidity on the creep and relaxation behaviour of a cement paste by micro-indentation techniques. *Cement and Concrete Research*, 91:39-51. https://doi.org/10.1016/j.cemconres.2016.10.005

Fu Q, Xie YJ, Long GC, et al., 2015. Temperature sensitivity and model of stress relaxation properties of cement and asphalt mortar. *Construction and Building Materials*, 84:1-11. https://doi.org/10.1016/j.conbuildmat.2015.03.064

Gallucci E, Zhang X, Scrivener KL, 2013. Effect of temperature on the microstructure of calcium silicate hydrate (C-S-H). *Cement and Concrete Research*, 53:185-195. https://doi.org/10.1016/j.cemconres.2013.06.008

Gao Y, Zhang J, Han P, 2013. Determination of stress relaxation parameters of concrete in tension at early-age by ring test. *Construction and Building Materials*, 41:152-164. https://doi.org/10.1016/j.conbuildmat.2012.12.004

Giorla AB, Dunant CF, 2018. Microstructural effects in the simulation of creep of concrete. *Cement and Concrete Research*, 105:44-53. https://doi.org/10.1016/j.cemconres.2017.12.001

Gowers RJ, Carbone P, 2015. A multiscale approach to model

hydrogen bonding: the case of polyamide. *The Journal of Chemical Physics*, 142(22):224907. https://doi.org/10.1063/1.4922445

Han GZ, Fang ZK, Chen MD, 2010. Modified Eyring viscosity equation and calculation of activation energy based on the liquid quasi-lattice model. *Science China Physics, Mechanics and Astronomy*, 53(10):1853-1860. https://doi.org/10.1007/s11433-010-4096-9

Hou DS, Ma HY, Yu Z, et al., 2014a. Calcium silicate hydrate from dry to saturated state: structure, dynamics and mechanical properties. *Acta Materialia*, 67:81-94. https://doi.org/10.1016/j.actamat.2013.12.016

Hou DS, Zhu Y, Lu YY, et al., 2014b. Mechanical properties of calcium silicate hydrate (C-S-H) at nano-scale: a molecular dynamics study. *Materials Chemistry and Physics*, 146(3):503-511. https://doi.org/10.1016/j.matchemphys.2014.04.001

Hou DS, Zhao TJ, Ma HY, et al., 2015a. Reactive molecular simulation on water confined in the nanopores of the calcium silicate hydrate gel: structure, reactivity, and mechanical properties. *The Journal of Physical Chemistry C*, 119(3):1346-1358. https://doi.org/10.1021/jp509292q

Hou DS, Zhang JR, Li ZJ, et al., 2015b. Uniaxial tension study of calcium silicate hydrate (C-S-H): structure, dynamics and mechanical properties. *Materials and Structures*, 48(11):3811-3824. https://doi.org/10.1617/s11527-014-0441-1

Hou DS, Li ZJ, Zhao TJ, et al., 2015c. Water transport in the nano-pore of the calcium silicate phase: reactivity, structure and dynamics. *Physical Chemistry Chemical Physics*, 17(2):1411-1423. https://doi.org/10.1039/C4CP04137B

Hou DS, Yu J, Jin ZQ, et al., 2018a. Molecular dynamics study on calcium silicate hydrate subjected to tension loading and water attack: structural evolution, dynamics degradation and reactivity mechanism. *Physical Chemistry Chemical Physics*, 20(16):11130-11144. https://doi.org/10.1039/C7CP08634B

Hou DS, Jia YT, Yu J, et al., 2018b. Transport properties of sulfate and chloride ions confined between calcium silicate hydrate surfaces: a molecular dynamics study. *The Journal of Physical Chemistry C*, 122(49):28021-28032. https://doi.org/10.1021/acs.jpcc.8b07484

Jana R, Pastewka L, 2019. Correlations of non-affine displacements in metallic glasses through the yield transition. *Journal of Physics: Materials*, 2(4):045006. https://doi.org/10.1088/2515-7639/ab36ed

Jennings HM, 2004. Colloid model of C-S-H and implications to the problem of creep and shrinkage. *Materials and Structures Aims*, 37(1):59-70. https://doi.org/10.1007/BF02481627

Kai MF, Zhang LW, Liew KM, 2021. New insights into creep characteristics of calcium silicate hydrates at molecular level. *Cement and Concrete Research*, 142:106366. https://doi.org/10.1016/j.cemconres.2021.106366

Li B, Li N, Brouwers HJH, et al., 2020. Understanding hydrogen bonding in calcium silicate hydrate combining solid-state NMR and first principle calculations. *Construction and Building Materials*, 233:117347. https://doi.org/10.1016/j.conbuildmat.2019.117347

Li J, Yu QJ, Huang HL, et al., 2019. Effects of Ca/Si ratio, aluminum and magnesium on the carbonation behavior of calcium silicate hydrate. *Materials*, 12(8):1268. https://doi.org/10.3390/ma12081268

Li X, Grasley ZC, Garboczi EJ, et al., 2015. Modeling the apparent and intrinsic viscoelastic relaxation of hydrating cement paste. *Cement and Concrete Composites*, 55:322-330. https://doi.org/10.1016/j.cemconcomp.2014.09.012

Li XD, Grasley ZC, Bullard JW, et al., 2018. Creep and relaxation of cement paste caused by stress-induced dissolution of hydrated solid components. *Journal of the American Ceramic Society*, 101(9):4237-4255. https://doi.org/10.1111/jace.15587

Li ZM, Zhang SZ, Liang XH, et al., 2020. Cracking potential of alkali-activated slag and fly ash concrete subjected to restrained autogenous shrinkage. *Cement and Concrete Composites*, 114:103767. https://doi.org/10.1016/j.cemconcomp.2020.103767

Liang CY, Zheng Q, Jiang JY, et al., 2022. Calcium silicate hydrate colloid at different humidities: microstructure, deformation mechanism, and mechanical properties. *Acta Materialia*, 228:117740. https://doi.org/10.1016/j.actamat.2022.117740

Liu WH, Zhang LW, Liew KM, 2020. Modeling of crack bridging and failure in heterogeneous composite materials: a damage-plastic multiphase model. *Journal of the Mechanics and Physics of Solids*, 143:104072. https://doi.org/10.1016/j.jmps.2020.104072

Lothenbach B, Scrivener K, Hooton RD, 2011. Supplementary cementitious materials. *Cement and Concrete Research*, 41(12):1244-1256. https://doi.org/10.1016/j.cemconres.2010.12.001

Manzano H, Pellenq RJM, Ulm FJ, et al., 2012. Hydration of calcium oxide surface predicted by reactive force field molecular dynamics. *Langmuir*, 28(9):4187-4197. https://doi.org/10.1021/la204338m

Manzano H, Masoero E, Lopez-Arbeloa I, et al., 2013. Shear deformations in calcium silicate hydrates. *Soft Matter*, 9(30):7333-7341. https://doi.org/10.1039/C3SM50442E

Maruyama I, Igarashi G, Nishioka Y, 2015. Bimodal behavior of C-S-H interpreted from short-term length change and water vapor sorption isotherms of hardened cement paste. *Cement and Concrete Research*, 73:158-168. https://doi.org/10.1016/j.cemconres.2015.03.010

Masoumi S, Zare S, Valipour H, et al., 2019. Effective interactions between calcium-silicate-hydrate nanolayers. *The Journal of Physical Chemistry C*, 123(8):4755-4766. https://doi.org/10.1021/acs.jpcc.8b08146

Morshedifard A, Masoumi S, Abdolhosseini Qomi MJ, 2018. Nanoscale origins of creep in calcium silicate hydrates. *Nature Communications*, 9(1):1785. https://doi.org/10.1038/s41467-018-04174-z

Mortazavi B, Javvaji B, Shojaei F, et al., 2021a. Exceptional piezoelectricity, high thermal conductivity and stiffness and promising photocatalysis in two-dimensional $MoSi_2N_4$ family confirmed by first-principles. *Nano Energy*, 82:105716. https://doi.org/10.1016/j.nanoen.2020.105716

Mortazavi B, Silani M, Podryabinkin EV, et al., 2021b. First-principles multiscale modeling of mechanical properties

in graphene/borophene heterostructures empowered by machine-learning interatomic potentials. *Advanced Materials*, 33(35):2102807. https://doi.org/10.1002/adma.202102807

Pellenq RJM, Kushima A, Shahsavari R, et al., 2009. A realistic molecular model of cement hydrates. *Proceedings of the National Academy of Sciences of the United States of America*, 106(38):16102-16107. https://doi.org/10.1073/pnas.0902180106

Pitman MC, van Duin ACT, 2012. Dynamics of confined reactive water in smectite clay–zeolite composites. *Journal of the American Chemical Society*, 134(6):3042-3053. https://doi.org/10.1021/ja208894m

Priezjev NV, 2017. Collective nonaffine displacements in amorphous materials during large-amplitude oscillatory shear. *Physical Review E*, 95(2):023002. https://doi.org/10.1103/PhysRevE.95.023002

Richardson IG, 1999. The nature of C-S-H in hardened cements. *Cement and Concrete Research*, 29(8):1131-1147. https://doi.org/10.1016/S0008-8846(99)00168-4

Rong H, Dong W, Zhao XY, et al., 2021. Investigation on multi-cracks initiation and propagation of fiber reinforced concrete in restrained shrinkage ring tests. *Theoretical and Applied Fracture Mechanics*, 111:102856. https://doi.org/10.1016/j.tafmec.2020.102856

Rossi P, 1997. Strain rate effects in concrete structures: the LCPC experience. *Materials and Structures*, 30(1):54-62. https://doi.org/10.1007/BF02539277

Scrivener KL, Kirkpatrick RJ, 2008. Innovation in use and research on cementitious material. *Cement and Concrete Research*, 38(2):128-136. https://doi.org/10.1016/j.cemconres.2007.09.025

Shahsavari R, Pellenq RJM, Ulm FJ, 2011. Empirical force fields for complex hydrated calcio-silicate layered materials. *Physical Chemistry Chemical Physics*, 13(3):1002-1011. https://doi.org/10.1039/C0CP00516A

Shimizu F, Ogata S, Li J, 2007. Theory of shear banding in metallic glasses and molecular dynamics calculations. *Materials Transactions*, 48(11):2923-2927. https://doi.org/10.2320/matertrans.MJ200769

Shishegaran A, Khalili MR, Karami B, et al., 2020. Computational predictions for estimating the maximum deflection of reinforced concrete panels subjected to the blast load. *International Journal of Impact Engineering*, 139:103527. https://doi.org/10.1016/j.ijimpeng.2020.103527

Talebi H, Silani M, Bordas SPA, et al., 2014. A computational library for multiscale modeling of material failure. *Computational Mechanics*, 53(5):1047-1071. https://doi.org/10.1007/s00466-013-0948-2

Tamtsia BT, Beaudoin JJ, 2000. Basic creep of hardened cement paste: a re-examination of the role of water. *Cement and Concrete Research*, 30(9):1465-1475. https://doi.org/10.1016/S0008-8846(00)00279-9

Tang C, Wong CH, 2015. Effect of atomic-level stresses on local dynamic and mechanical properties in Cu_xZr_{100-x} metallic glasses: a molecular dynamics study. *Intermetallics*, 58:50-55. https://doi.org/10.1016/j.intermet.2014.11.006

Tian HW, Stephan D, Lothenbach B, et al., 2021. Influence of foreign ions on calcium silicate hydrate under hydrothermal conditions: a review. *Construction and Building Materials*, 301:124071. https://doi.org/10.1016/j.conbuildmat.2021.124071

Todd BD, Daivis PJ, 2017. Nonequilibrium Molecular Dynamics: Theory, Algorithms and Applications. Cambridge University Press, Cambridge, UK. https://doi.org/10.1017/9781139017848

Vandewalle L, Nemegeer D, Balazs L, et al., 2002. Design of steel fibre reinforced concrete using the *σ-w* method: principles and applications. *Materials and Structures*, 35: 262-278. https://doi.org/10.1007/BF02482132

Venkovic N, Sorelli L, Martirena F, 2014. Nanoindentation study of calcium silicate hydrates in concrete produced with effective microorganisms-based bioplasticizer. *Cement and Concrete Composites*, 49:127-139. https://doi.org/10.1016/j.cemconcomp.2013.12.003

Wang JW, Kalinichev AG, Kirkpatrick RJ, 2004. Molecular modeling of water structure in nano-pores between brucite (001) surfaces. *Geochimica et Cosmochimica Acta*, 68(16):3351-3365. https://doi.org/10.1016/j.gca.2004.02.016

Wang XF, Bao YW, Liu XG, et al., 2015. The stress relaxation of cement clinkers under high temperature. *Frontiers of Mechanical Engineering*, 10(4):413-417. https://doi.org/10.1007/s11465-015-0357-7

Wang ZP, Chen YT, Xu LL, et al., 2022. Insight into the local C-S-H structure and its evolution mechanism controlled by curing regime and Ca/Si ratio. *Construction and Building Materials*, 333:127388. https://doi.org/10.1016/j.conbuildmat.2022.127388

Yang XS, Wang YJ, Wang GY, et al., 2016. Time, stress, and temperature-dependent deformation in nanostructured copper: stress relaxation tests and simulations. *Acta Materialia*, 108:252-263. https://doi.org/10.1016/j.actamat.2016.02.021

Youssef M, Pellenq RJM, Yildiz B, 2011. Glassy nature of water in an ultraconfining disordered material: the case of calcium–silicate–hydrate. *Journal of the American Chemical Society*, 133(8):2499-2510. https://doi.org/10.1021/ja107003a

Zhang MZ, Ye G, van Breugel K, 2011. Microstructure-based modeling of water diffusivity in cement paste. *Construction and Building Materials*, 25(4):2046-2052. https://doi.org/10.1016/j.conbuildmat.2010.11.042

Zhang T, Qin WZ, 2006. Tensile creep due to restraining stresses in high-strength concrete at early ages. *Cement and Concrete Research*, 36(3):584-591. https://doi.org/10.1016/j.cemconres.2005.11.017

Zhang Y, Zhou Q, Ju JW, et al., 2021. New insights into the mechanism governing the elasticity of calcium silicate hydrate gels exposed to high temperature: a molecular dynamics study. *Cement and Concrete Research*, 141: 106333. https://doi.org/10.1016/j.cemconres.2020.106333

Zheng Q, Jiang JY, Li XL, et al., 2021. In situ TEM observation of calcium silicate hydrate nanostructure at high temperatures. *Cement and Concrete Research*, 149:106579. https://doi.org/10.1016/j.cemconres.2021.106579